KSCE Journal of Civil Engineering (2022) 26(4):1966-1977
DOI 10.1007/s12205-022-1414-5

pISSN 1226-7988, eISSN 1976-3808
www.springer.com/12205

Tunnel Engineering

Relationship between Invert-Filling Disengaging and Deformation of Shield Tunnel Using Staggered Assembled Segment

Hao Jin[a,b], **Jie Su**[b], **and Chen Zhao**[c]

[a]*School of Transportation, Southeast University, Nanjing 211189, China*
[b]*Key Laboratory of Urban Underground Engineering of Ministry of Education, Beijing Jiaotong University, Beijing 100044, China*
[c]*The Key Laboratory of Road and Traffic Engineering, Ministry of Education, Tongji University, Shanghai 201804, China*

ARTICLE HISTORY

Received 12 August 2021
Revised 11 November 2021
Accepted 22 November 2021
Published Online 15 January 2022

KEYWORDS

Subway
Shield tunnel
Invert filling disengaging
Tunnel deformation
Staggered assembled segment

ABSTRACT

The disengaging between invert filling and segment affects the safety of train operation. A 3D numerical model of a three-ring staggered assembled shield tunnel is established, which is verified by a full-scale test. On this basis, cohesive element is inserted between the invert filling and tunnel segment to simulate the fracture process of invert filling-segment interface, and explore the relationship between the deformation of staggered assembled shield tunnel and the disengaging of invert filling. The results show that: 1) The development of invert filling disengaging affects the internal forces of shield tunnel segments. 2) The relationship between the development of invert filling disengaging and the deformation of shield tunnel can be four stages. Different segment assembly methods do not affect the variability of the disengaging ratio. Tensile failure occurs in 89% of the interface layer, which is the main form of invert filling disengaging. 3) The relationship between the development of disengaging distance and the deformation of shield tunnel also can be four stages. The faster the horizontal convergent deformation develops in the segment assembly method, the slower the growth rate of the disengaging distance. 4) The faster the horizontal convergent deformation develops in the segment assembly method, the slower the growth rate of the disengaging volume.

1. Introduction

The invert filling is directly poured on the segment (Jin et al., 2022), and the bonding strength of its contact interface is low. When the shield tunnel is greatly deformed, the deformation between the segment and invert filling is not coordinated, which leads to the peeling between the two, resulting in the formation of disengaging, which affects the support of the track and endangers the safety. Uneven deformation often occurs in shield tunnel, especially in soft stratum (Liu et al., 2021). Adjacent construction (Shi et al., 2016; Liang et al., 2018; Jin et al., 2019), groundwater leakage (Gao et al., 2019; Huang et al., 2020; Wu et al., 2020), traffic loading (Yan et al., 2018; Yi et al., 2019; Li et al., 2020b), effect of uneven subsoil (Shen et al., 2014; Wu et al., 2017) will cause large deformation of shield tunnel, which can cause a variety of diseases (Zhang et al., 2020), such as segment crack, steel corrosion, water leakage, joint opening. etc. (Shao et al., 2016; Dong et al., 2017; Wang et al., 2020; Jin and Yu, 2022) Theoretical, experimental and numerical methods have been used to analyze the relationship between deformation of shield tunnel and structural damage. There are researches of using theoretical analysis means, such as Wu (Wu et al., 2015) proposes a shield tunnel model, considering the shear dislocation between rings and the bending deformation and shear deformation of beams. Zheng (Zheng et al., 2005) based on the equivalent axial stiffness model and researched the relationship between the joint opening of tunnel segments and the longitudinal deformation curvature. There are researches using numerical simulation analysis, such as Wang (Wang and Zhang, 2013) studied the developing law of horizontal deformation of tunnels under overload and the relationship between variation of tunnel diameter and bolt stress, concrete stress and joint opening is established. Zhu (2014) studied the deformation law of the tunnel cross section and established the relationship between the horizontal diameter deformation and the maximum joint opening, the maximum bolt stress, and the maximum concrete stress under different assembly

CORRESPONDENCE Hao Jin ✉ jinhao@seu.edu.cn School of Transportation, Southeast University, Nanjing 211189, China; Key Laboratory of Urban Underground Engineering of Ministry of Education, Beijing Jiaotong University, Beijing 100044, China

methods. There are researches using experimental analysis, such as Molins (Molins and Arnau, 2011) conducted a full-scale field test on the Barcelona Metro shield tunnel, which considered the interaction between structure and soil and the mechanical response of the segment structure under hard soil conditions was obtained. Bi (Bi et al., 2014) conducted multiple sets of full-scale tests on a single ring to study the ultimate deformation capacity, stress state and failure process of the tunnel structure under ground load, ground overload, and surrounding unloading. The above studies mostly focused on exploring the relationship between shield tunnel deformation and joint openings, water leakage, segment damage and other diseases, but seldom studied the relationship between the tunnel invert filling disengaging and tunnel deformation.

The researches on the invert filling disengaging mostly focus on the treatment measures, detection methods and the analysis of the force characteristics of the invert filling after disengaging. The treatment measures for the invert filling disengaging mainly include grouting reinforcement (Li et al., 2020a), invert filling renovation (Ji and Chen, 2019), etc. The detection methods of disengaging mainly include traditional methods such as empirical judgment method, drilling core method and geological radar method. Liu (Liu et al., 2015) proposed the calculation method of calculating the disengaging of invert filling by hydrostatic leveling sensor. The analysis of the force characteristics of the invert filling after disengaging mainly include: Ji (2014) analyzed the force and deformation characteristics of the invert filling under train load when there are voids and disengaging at the bottom of the invert filling, and on this basis, carried out the research on the safety evaluation standard of the invert filling. Gong (Gong et al., 2020) analyzed the influence of grouting layer stiffness and contact surface bonding strength on the occurrence and evolution of the disengaging. At present, there are few studies on the mechanical characteristics of the interface between invert filling and segment, especially the effect of shield tunnel's deformation on the mechanical characteristics of the contact layer between them. Relevant measured data shows that with the increase of tunnel deformation, the disengaging of invert filling tends to increase (Zhang et al., 2020). This paper explores the relationship between invert filling disengaging and deformation of shield tunnel with staggered assembled segment through numerical simulation, and explains the development process of the disengaging.

This paper studies the relationship between the deformation of the shield tunnel structure with different assembly methods and the disengaging of invert filling, including disengaging ratio, disengaging distance, and disengaging volume. Section 2 introduces the numerical model of three-ring staggered shield tunnel, and verifies the model by a full-scale test. Section 3 introduces the insertion method of the numerical model of invert filling. Section 4 introduces five different assembly methods of shield tunnel, namely five working conditions. Section 5 analyzes the changing law of shield tunnel deformation under five working conditions. Section 6 analyzes the relationship between shield tunnel deformation and the development of disengaging and analyzes the failure mode of the interface layer. Section 7 and 8 respectively analyze the relationship between disengaging distance and disengaging volume under 5 working conditions.

2. Modelling Methods and Verification

Based on the segment structure design Nanjing Metro, a FEM model of three-ring staggered assembled shield tunnel is established, which is verified by the results of full-scale test.

2.1 Modelling Method

2.1.1 Geometric Model

The inner radius of the shield tunnel is 2.75 m, the outer radius is 3.1 m and the segment width is 1.2 m. One sealing segment, two adjacent segments and three standard segments comprise a single tunnel ring. The center angle of three types of segments are 21.5°, 68° and 67.5°. The shield tunnel adopts staggered assembly and the position of the sealing segment between adjacent rings deviates by 22.5°. The segment arrangement is shown in Fig. 1.

There are 12 bolts in the longitudinal joints in one ring and 16 bolts in the circumferential joints between the two rings. The bolt hole, the caulking groove and sealing groove are neglected for simplicity, as shown in Fig. 2. The segment rebars include main steel bar, longitudinal steel bar and stirrup.

2.1.2 Material Properties

The concrete grade of segments is C50, Young's Modulus is 34.5 GPa and Poisson's ratio is 0.2. The three-fold line is used to

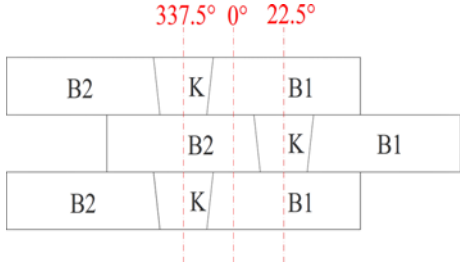

Fig. 1. Segment Arrangement

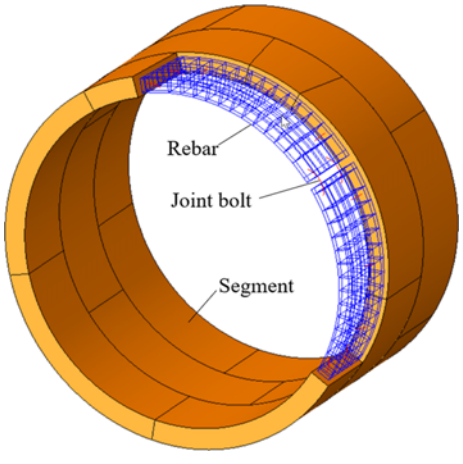

Fig. 2. Three-Ring Shield Tunnel FEM Model

Table 1. Parameters of Bolts and Rebars (Jin et al., 2018)

Material	Young's Modulus E (GPa)	Poisson's ratio μ	Yield strength f_y (MPa)	Tensile strength f_{st} (MPa)
Bolts	200	0.3	400	500
Rebars of HPB235	210	0.3	235	370
Rebars of HRB335	200	0.3	335	455

characterize the elastoplastic characteristics of bolts and rebars to simulate the yielding, hardening and softening during loading, and the parameters of bolts and rebars are shown in Table 1.

2.1.3 Element and Interaction Properties

The segments are modelled as 3D stress element (C3D8). The bolts can bear tensile and shear forces and the beam element (B31) is used for simulation, whose section is consistent with the real bolt section. The repairs are modelled as truss element (T3D2).

The General Contact is set for the interaction between segments. The normal behavior is "Hard" contact. The tangential behavior is penalty, whose friction coefficient is 0.5.

"Embedded Region" is used to embed the reinforcements and bolts into the segment without considering the slip between the two.

2.1.4 Load Conditions and Boundary Conditions

This paper considers the weight of the rebars and the design load of the shield tunnel. The tunnel depth is 16 m. The soil condition is shown in Fig. 3. The earth pressure pattern is shown in Fig. 4. The unit weight of the soil is 18.1 kN/m^3, 17.5 kN/m^3 and 18.2 kN/m^3. The horizontal earth pressure coefficient (λ) is 0.42, 0.70 and 0.53. P1 is the pressure of soil and water above the shield tunnel. P5 is the average self-weight of the shield tunnel. The reaction pressure at the tunnel bottom is P2, which equal to P1 plus P5. P3 and P4 are the lateral earth pressure horizontally on the top and bottom of the tunnel, respectively, which are obtained

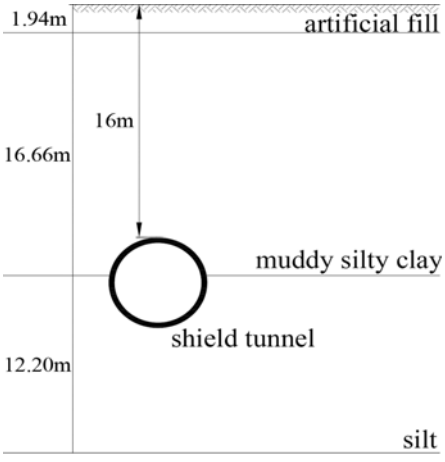

Fig. 3. Soil Conditions

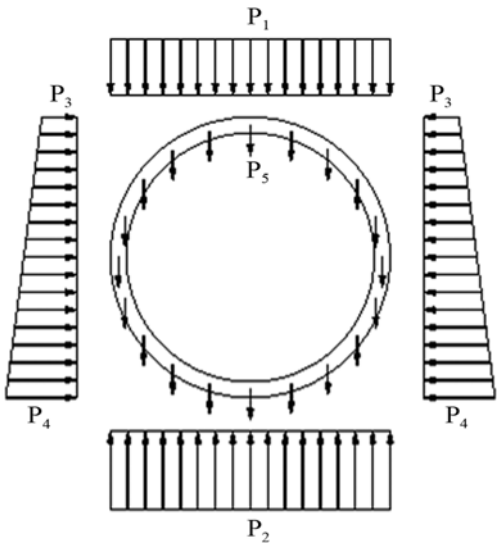

Fig. 4. Earth Pressure Distribution Pattern around Tunnel

by multiplying vertical earth pressure multiplied by the horizontal earth pressure coefficient. In order to simulate the real deformation shape of the shield tunnel, overloading is applied to the tunnel structure by increasing P1 and P2 to obtain a larger convergent deformation. Every 0.1 loading history represents one time of design load, and the final load is 10 times of design loads. The horizontal displacement of the model is restricted at the top and bottom of the model, the vertical displacement of the model is restricted at the arch waist of the segment, and the longitudinal displacement of the model is restricted at both ends of the segment to limit the displacement and rotation of the model.

2.2 Verification by Full-Scale Experiment

2.2.1 Test Device

The loading system is composed of reaction frame, load-holding beam, jack and vertical support system as shown in Fig. 5. The reaction frame is composed of three main reaction rings and auxiliary connecting parts. Each reaction ring is composed of a

Fig. 5. Test System

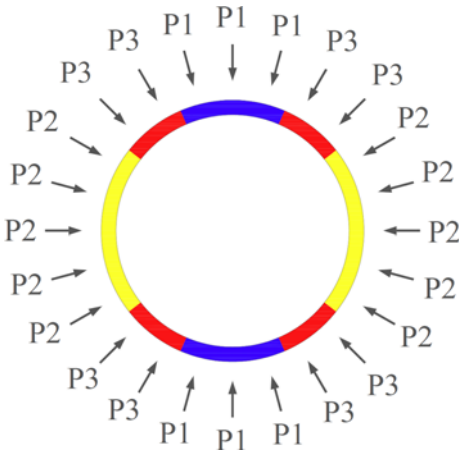

Fig. 6. Loading Points

horizontal web ring and two vertical flange rings, and is thickened at the loading position of the jack. The whole reaction frame constitutes a self-balancing system.

2.2.2 Loading Scheme

Totally 24 loading points are designed to simulate the loads around the tunnel. As shown in Fig. 6, the 24 loading points are six P1, ten P2, and eight P3. P1 is used as the vertical soil pressure, water pressure, self-weight and reaction pressure. P2 stands for the coefficient of the horizontal earth pressure, which is equal to $\lambda \times$ P1. P3 stands for the soil resistance pressure, which is equal to $0.5 \times (P1 + P2)$.

The design values of P1, P2 and P3 are calculated according to the typical calculating section in section 2.1.4. Under the buried depth of 16 m, P1 = 280 kN, P2 = 196 kN, P3 = 238 kN. The loading process is divided into two stages. ① P1 is loaded in stages from 0kN to F2. Meanwhile, P2 and P3 are P2 = $\lambda \times$ P1, P3 = $0.5 \times$ (P1 + P2). The load increment of each level of P1 is 0.1 times of F1. ② P1 is loaded in stages from F2 to F1. Meanwhile, P2 and P3 are P2 = $\lambda \times$ P1, P3 = $0.5 \times$ (P1 + P2). The load increment of each level of P1 is 0.05F1. F1 is the design load of P1 when the depth of shield tunnel is 16m, and F2 is 0.8 times F1, which is 224 kN.

2.2.3 Measuring Points and Measuring Contents

Measure the convergent deformation of the shield tunnel with a rope displacement meter. Considering that the upper and lower rings are symmetrical along the middle ring, the analysis of the deformation of the middle ring is emphasized. There are 8 and 16 displacement sensors on the upper and middle ring respectively, for a total of 24 (D1 – D24).

The stress of the main rebar is measured by the rebar stress gauges which is welded with the main rebar of the segment in advance before pouring concrete. The rebar stress gauges are arranged at two points on the inner and outer main rebar of the same section. The upper ring and the middle ring each have 4 cross sections, and a total of 16 rebar stress gauges. Fig. 7 shows the distribution of rebar stress gauges.

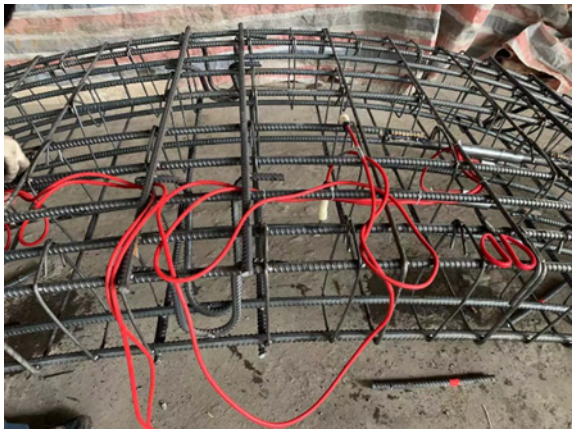

Fig. 7. Rebar Stress Gauges

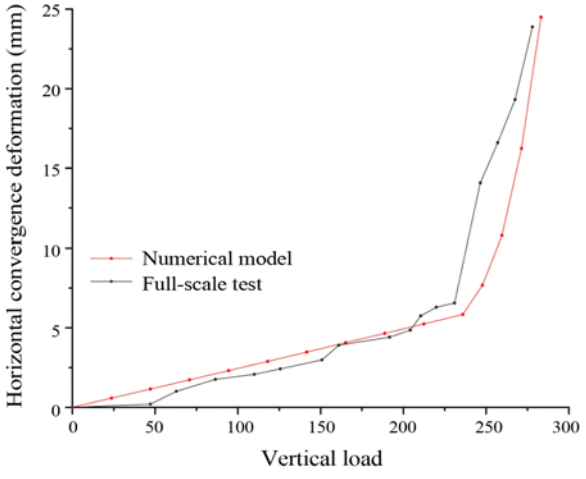

Fig. 8. Deformation Comparison Between Full-Scale Test and Numerical Model

2.2.4 Finite Element Model Verification

Figure 8 shows the horizontal convergence deformation of shield tunnel for numerical model and full-scale test. The abscissa is P1 in the full-scale test and the vertical water and earth pressure in the numerical model. When the jack load P1 is transformed into a uniform load on the segment, its value is the same as the vertical soil and water pressure in numerical model. The load-deformation curve obtained by the numerical method mainly fit the full-scale test results.

Figure 9 shows the stress-load curve of the inner and outer main rebars at the 0° section position in the numerical model and full-scale test. The tension of rebar is positive and the compression is negative. Fig. 10 shows the strain-load curve of the inner and outer main rebars at the 236° section position in the numerical model and full-scale test. The stress, strain of rebars obtained by the numerical method mainly fit the full-scale test results.

Comparing the above three figures, the numerical model results are slightly different from the full-scale test results. The reason is that in the full-scale test, rebars are affected by material properties, welding, segment pouring and maintenance, and their

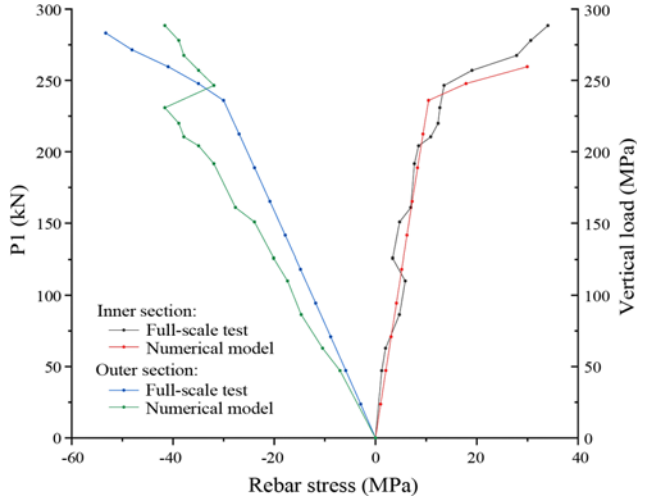

Fig. 9. Rebar Stress Comparison between Full-Scale Test and Numerical Model

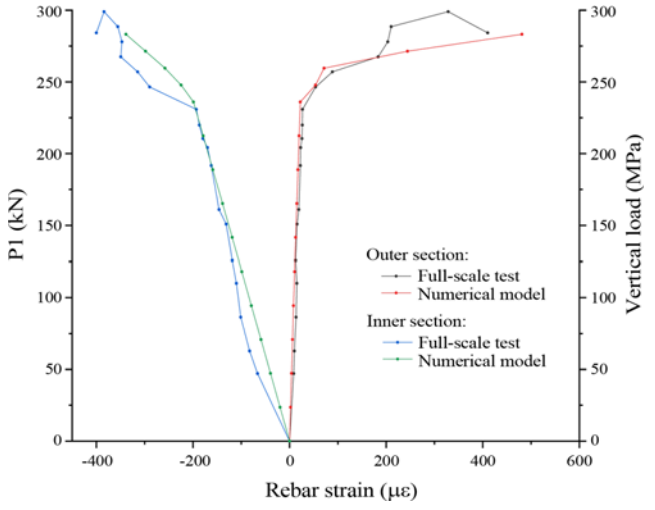

Fig. 10. Rebar Strain Comparison between Full-Scale Test and Numerical Model

stress state is not as ideal as the numerical model assumes. Generally speaking, the deformation of shield tunnel and stress-strain law of the rebars obtained by numerical model agree well with the full-scale test results, which proves the correctness and rationality of the FEM model of the three-ring staggered assembled shield tunnel.

3. Numerical Model of Invert Filling

The invert filling is added into the three-ring staggered assembled shield tunnel model established in Section 2.2 with a height of 0.6 m. The design of drainage structure is not considered. The concrete grade of invert filling is C35, whose Young's Modulus is 31.4 GPa and Poisson's ratio is 0.2. The invert filling is modelled as 3D stress element (C3D8), as shown in Fig. 11. FEM and meshfree method (Rabczuk and Belytschko, 2004, 2007; Rabczuk et al., 2008) are widely used in the simulation of crack initiation and crack growth. The invert filling-segment interface is one of the new-to-old concrete interfaces. Under load, the crack will develop along the interface. Therefore, the cohesive element is used to simulate the growth of directional cracks. Zero thickness cohesive elements (COH3D8) are inserted between the invert filling and tunnel segment to simulate the complex non-linear fracture process of invert filling-segment interface.

Figure 12 shows a bilinear traction-separation constitutive curve with a softening section, where n, s, t represent the normal direction and the two shear directions respectively. $\delta_n^0(\delta_s^0, \delta_t^0)$, $\delta_n^f(\delta_s^f, \delta_t^f)$ represent the initial damage displacement and failure

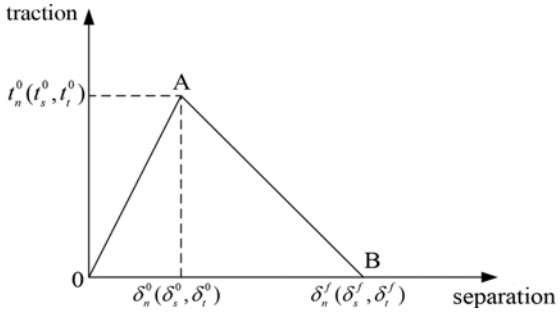

Fig. 12. Traction-Separation Constitutive

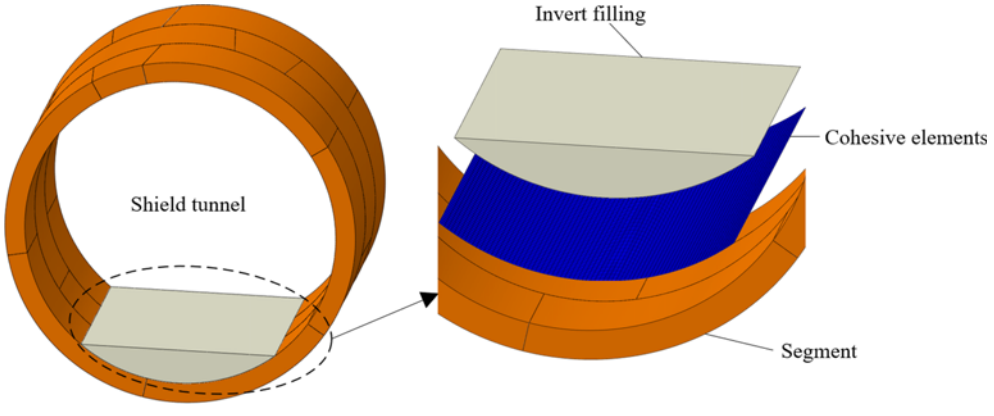

Fig. 11. Numerical Model of Invert Filling

displacement respectively. $t_n(t_s, t_t)$ represents the peak value of the nominal stress when the deformation is completely perpendicular to the interface or completely perpendicular to the first or second shear direction. G represents the fracture energy, which is the area enclosed by the triangle OAB in the figure. Before the damage, a linear elastic rising section is assumed to simulate the undamaged material. After the stress reaches the maximum value, as the loading continues, cracks begin to initiate and grow, and the stress begins to show a monotonous downward trend with the increase of displacement, until the stress decreases to zero.

The Quadratic nominal stress criterion is used as the initial damage criterion for the cohesive element. Damage initiates when a quadratic interaction function involving the nominal stress ratios reaches one. The criterion can be represented as

$$\left\{\frac{\langle t_n \rangle}{t_n^0}\right\}^2 + \left\{\frac{t_s}{t_s^0}\right\}^2 + \left\{\frac{t_t}{t_t^0}\right\}^2 = 1, \tag{1}$$

$< >$ is used to signify that the stress state or a pure compressive deformation does not initiate damage.

In order to describe the damage evolution of cohesive element, the equivalent displacement δ_m is introduced, which is given by

$$\delta_m = \sqrt{\langle \delta_n \rangle^2 + \delta_s^2 + \delta_t^2}. \tag{2}$$

For the bilinear traction-separation constitutive model, ABAQUS defined D to describe the damage evolution in the softening stage, which is given by

$$D = \frac{\delta_m^f \left(\delta_m^{\max} - \delta_m^0\right)}{\delta_m^{\max} \left(\delta_m^f - \delta_m^0\right)}, \tag{3}$$

where δ_m^f and δ_m^0 represent the effective displacement at total failure and the initiation of damage respectively. $\delta_m^{\max}$ represents the maximum effective displacement during the loading history.

The dependence of the fracture energy of the mode mix can be defined based on a power law fracture criterion. It is given by

$$\left\{\frac{G_n}{G_n^C}\right\}^\alpha + \left\{\frac{G_s}{G_s^C}\right\}^\alpha + \left\{\frac{G_t}{G_t^C}\right\}^\alpha = 1, \tag{4}$$

where G_n^C, G_s^C and G_t^C are the critical fracture energies required to cause failure in the normal, the first, and the second shear directions respectively. α is the material parameter for power law.

The material parameters used in the interface layer are: $t_n^0 = 4$ MPa, $t_s^0 = t_t^0 = 15$ MPa, $G_n^C = 100$ J/m^2, $G_s^C = G_t^C = 1{,}000$ J/m^2. Elastic stiffness is 10^7 MPa/m.

4. Staggered Assembly Conditions

In this paper, five shield tunnel assembly methods are set up. Through the overall rotation of the tunnel, the position of the center line of the tunnel is changed, different shield tunnel assembly methods are realized, and the influence of the position of the longitudinal joint on the relationship between the convergence deformation and the development of invert tunnel disengaging is explored. Under 5 conditions, the shield tunnel is rotated around

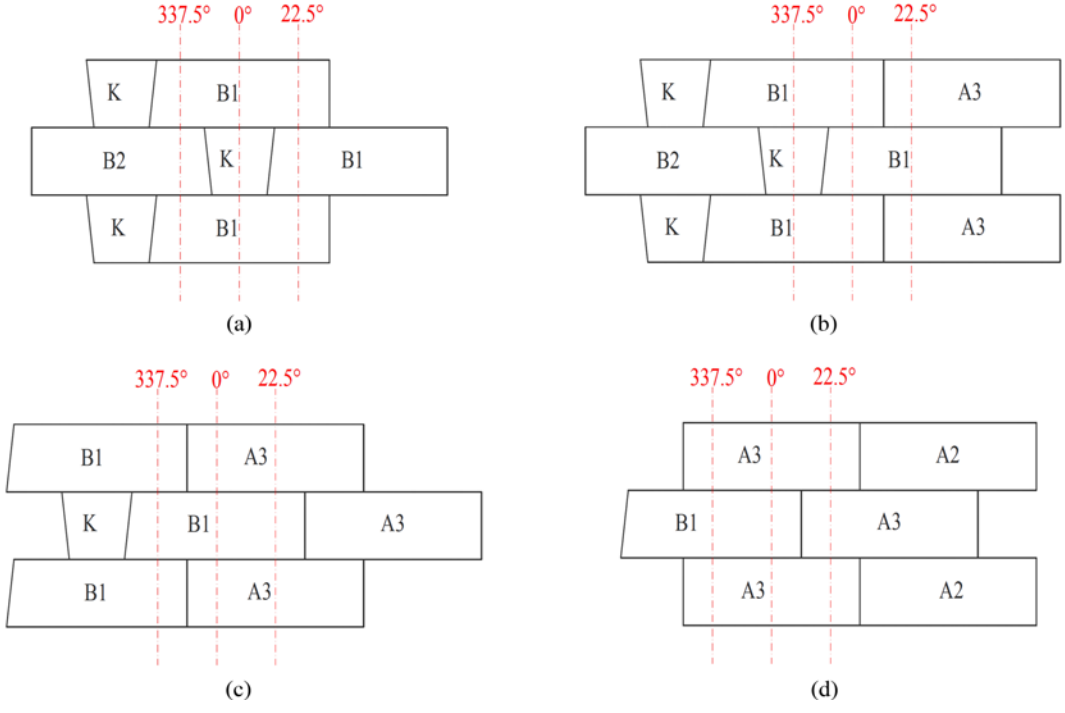

Fig. 13. Assembly Method for Each Working Condition: (a) Condition 1, (b) Condition 2, (c) Condition 3, (d) Condition 4

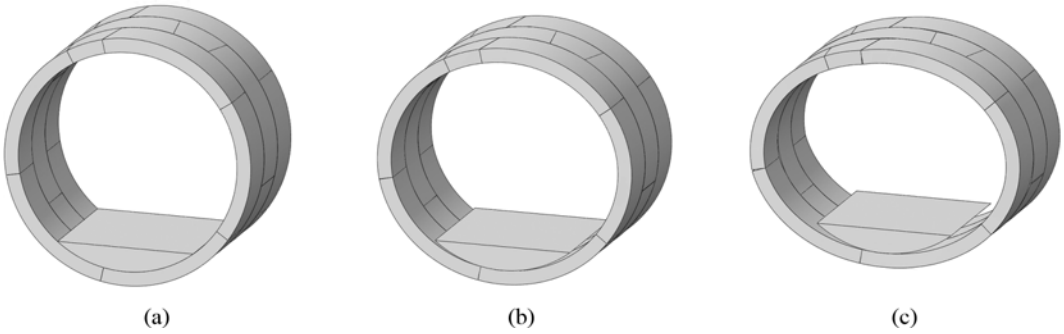

Fig. 14. Convergence Deformation of Shield Tunnel (5 times amplified): (a) Load = 0.1, (b) Load = 0.5, (c) Load = 1.0

the center by 0°, 22.5°, 45°, 67.5° and 90° respectively, which are namely as condition1, condition2, condition3, condition4 and condition5. The assembly methods of shield tunnels under 5 conditions are shown in Fig. 13.

5. The Influence of Segment Assembly Method on Convergence Deformation

Figure 14 shows the convergence deformation of the shied tunnel under different loads. When the load increases, the convergence deformation of shield tunnel increases gradually. Fig. 15 shows the horizontal convergence deformation of shield tunnels under 5 conditions. With the load increases, the growth trend of the convergent deformation of each condition is the same, and the difference lies in its magnitude. The curve can be divided into four parts. In stage I, the horizontal convergent deformation of the five conditions is less than 13.5 mm, and the development of the deformation increases linearly with the load. In stage II, the development speed of horizontal convergent deformation increases, and the curve is concave. When the horizontal convergent deformation reaches about 40 mm, it enters stage III. At this time, the growth rate of horizontal convergent deformation slows down, the curve is convex, and soon enters stage IV, where the development speed of horizontal

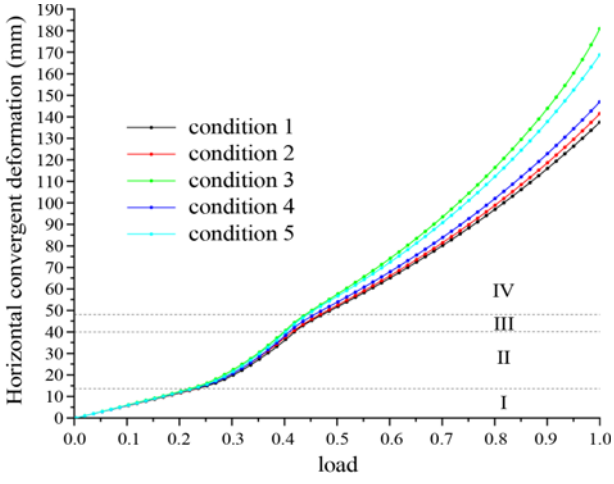

Fig. 15. Development of Horizontal Convergence Deformation

convergent deformation increases again. In stage II, III and IV, the development speed of horizontal convergence deformation of shield tunnel is different under different assembly modes. The development speed of horizontal convergence deformation is the slowest in condition 1, and the fastest in condition 3. Finally, the horizontal convergent deformation of condition 3 is 180.9 mm, and 137.5 mm for condition 1.

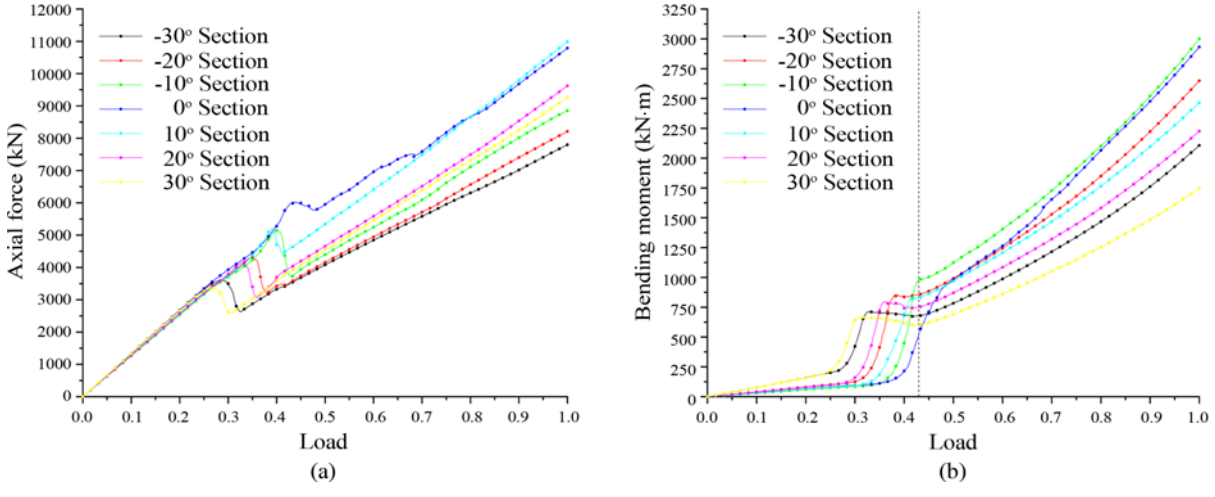

Fig. 16. Internal Force Change of Segment under Condition 1: (a) Axial Force, (b) Bending Moment

From the center of the invert filling to its both edges, a total of 7 sections are divided every 10°, and the axial force and bending moment of the segment on the split section under the loading process are intercepted. The direction of the axial force is perpendicular to the cross section, and the compression is positive. The bending moment is positive when the outer side of the segment is compressed and the inner side is tensioned.

Figure 16 shows the change process of segment internal force with load increase under condition 1. The internal force increases linearly with load increase. When the disengaging develops to the section, the axial force decreases and the bending moment increase faster. The axial force of the segment increases linearly after the disengaging edge crosses the section. For the bending moment, except for the 0° section, the bending moment of the other sections slowly decreases until the loading history reaches 0.43, and then the bending moment of each section continues to increase.

Figure 17 shows the change of the internal force of the segment at 30° section of each condition with increasing load. The changing trend of the internal force is the same in each condition, and the difference lies in its magnitude. The internal force first increases linearly. When the disengaging develops to the section, the axial force decreases and the bending moment increase faster. When the disengaging edge crosses the section, the segment axial force increases linearly with the load and the bending moment decreases until the load history reaches 0.43, and then the bending moment continues to increase with the increase of the load. The bending moment of condition 2 is the smallest among the five working conditions, while the axial force is the largest among them.

6. Relationship between Disengaging Development and Deformation

The development process of invert filling disengaging can be characterized by disengaging ratio, which is the ratio of disengaged interface layer area to the original area. Taking condition 1 as an example, the red part in Fig. 18 is the interface layer that is still stuck together, and the blue part is the disengaged layer. The disengaging of invert filling first occurred at the boundary of the layer. With the increase of horizontal convergence deformation, the disengaging boundary develops in the center of the invert filling in a parallel way. When the disengaging ratio reaches 99%, the disengaging will not develop.

Figure 19 shows the relationship between the disengaging ratio and the convergence deformation of shield tunnel under

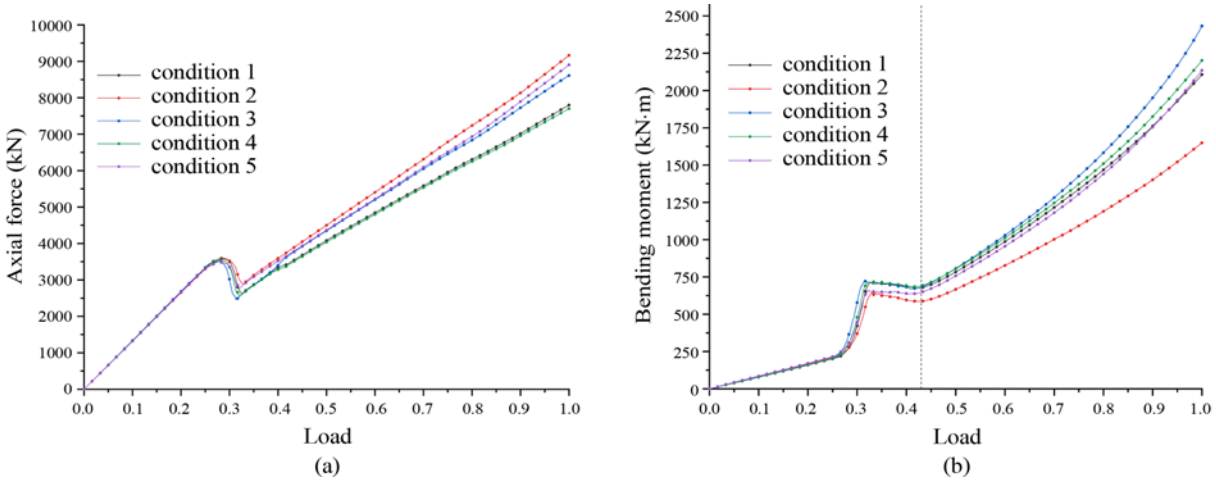

Fig. 17. Internal Forces of the Segment at 30° Section of Each Condition: (a) Axial Force, (b) Bending Moment

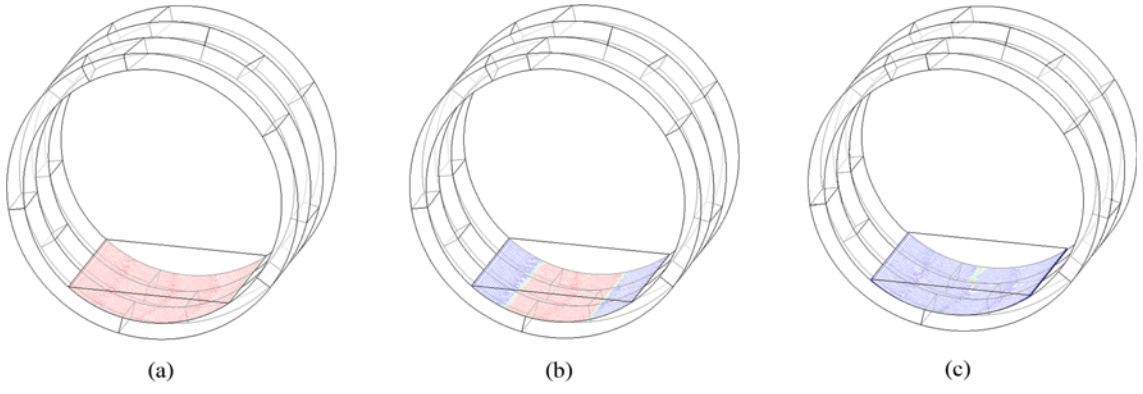

Fig. 18. Disengaging Diagram of Invert Filling: (a) Disengaging Ratio = 1.13%, (b) Disengaging Ratio = 50.61%, (c) Disengaging Ratio = 99.02%

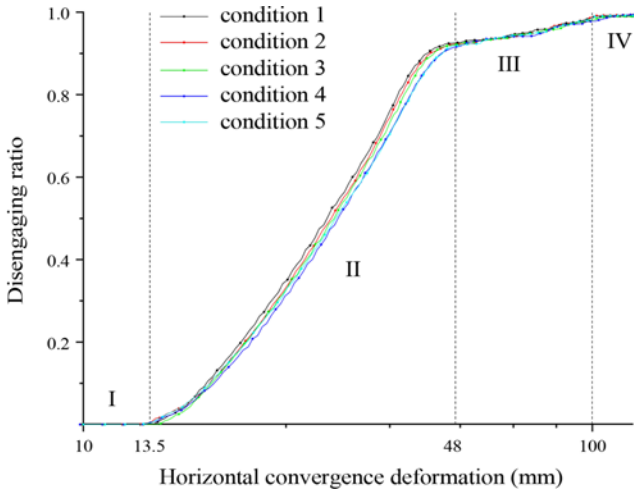

Fig. 19. Relationship between the Disengaging Ratio and the Convergence Deformation

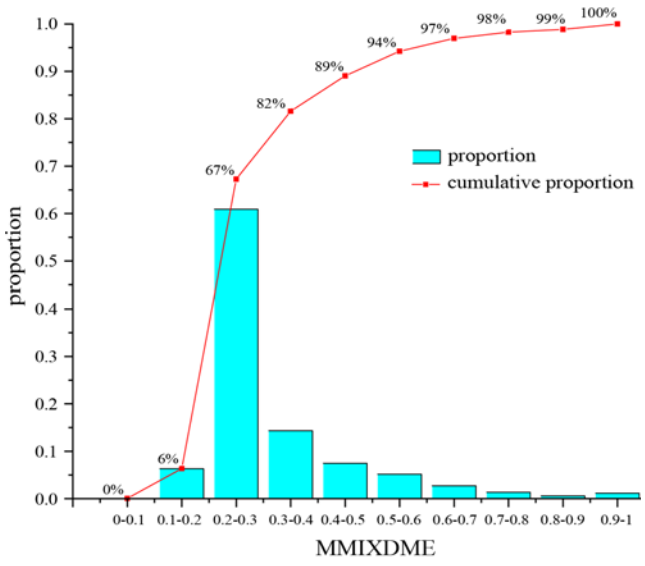

Fig. 20. MMIXDME Statistical

five conditions. The curve can be divided into four stages. In stage I, when the convergence deformation is less than 13.5 mm, disengaging does not occur. Stage II is the stage in which the convergence deformation is less than 48 mm under five working conditions, and the void rate is about 90%. Fitting the curve at this stage, the slope of the linear regression equation are 0.0280, 0.0277, 0.0261, 0.0271 and 0.02573, R^2 are 0.99445, 0.99667, 0.99573, 0.99439 and 0.99499, respectively. Therefore, in stage II, the disengaging ratio increases linearly with the horizontal convergence deformation of the shield tunnel. When entering stage III, the disengaging rate slows down. When the horizontal convergence deformation reaches about 100 mm, the disengaging rate of five conditions reaches the maximum value of about 99%. Then the curve enters stage IV, and the disengaging rate no longer increases with the convergence deformation. Under these five conditions, although the development speed of horizontal convergence deformation is different, the variation law of disengaging ratio with deformation is basically the same, that is, the disengaging ratio is basically the same under the same horizontal convergence deformation. Therefore, the assembly method does not affect the growth law of disengaging ratio.

According to the displacement mode of the crack surface, cracks can be divided into three types: type I (tension type), type II (slip type), and type III (tear type). When the shield tunnel is deformed, the interface between invert filling and segment is in a complex stress state. At this time, the cracking form of the interface layer is a mixed mode with multiple crack types. In this study, the damage evolution law of the interface layer is defined by the energy based mixing criterion, and the failure mode of the invert filling-segment interface under complex stress state is studied. By calculating the ratio of the tear energy release rate with respect to the total energy release rate, the relative ratio of tensile deformation (or shear deformation) can be quantified. According to the statistics of mode mix ratio during damage evolution, the main failure modes of the interface layer between invert filling and segment are determined. When MMIXDME is between 0 and 0.5, the cohesive elements are controlled by tensile damage, which leads to tensile cracks. Otherwhile the cohesive elements are controlled by shear damage (shear cracks) when the value is between 0.5 and 1. When MMIXDME is 1, the cohesive elements are not damaged yet (Han et al., 2020; Dagorn et al., 2021; Xiao et al., 2021). Taking condition1 as the research object, the MMIXDME value of the interface layer was counted with an interval of 0.1,an shown in Fig. 20. 89% of the interface layer have a tensile failure, 11% of the interface layer have a shear failure. The tensile failure is the main form of invert filling disengaging.

7. Relationship between Disengaging Distance and Deformation

The disengaging distance is the shortest distance between the edge of invert filling and the segment, which is represented by "d" in Fig. 21. Fig. 22 shows the relationship between the disengaging distance and the horizontal convergence deformation under 5 conditions. The variation trend of disengaging distance with the growth of convergence deformation is the same, but the growth rate is different. Combined with the analysis of section 4, the faster the development of deformation, the slower the growth rate of disengaging distance. The curve can be divided into four stages. In stage I, the convergence deformation is less than 13.5 mm. There is no disengaging so the disengaging distance is zero. In stage II, the development speed of the disengaging distance increases, and the curve is concave. When the horizontal convergent deformation reaches about 40 mm, it enters stage III, the growth rate of the disengaging distance slows down, and the curve is convex. When the convergent deformation reaches 48 mm, it enters stage IV, after which the disengaging distance increases linearly with the horizontal convergent deformation of the

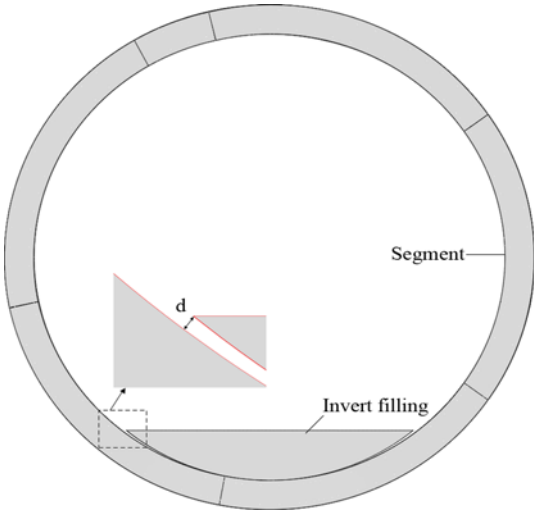

Fig. 21. Disengaging Distance

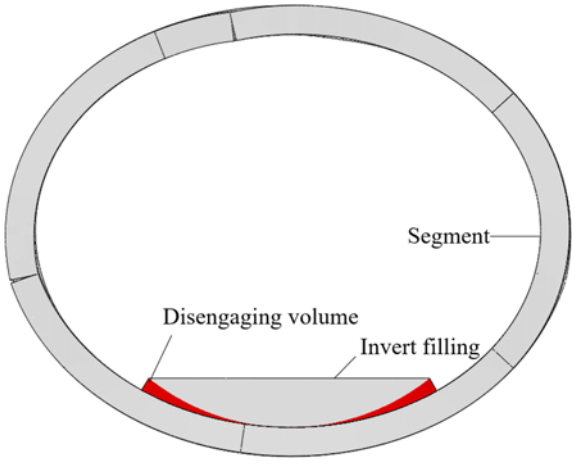

Fig. 23. Disengaging Volume (5 times amplified)

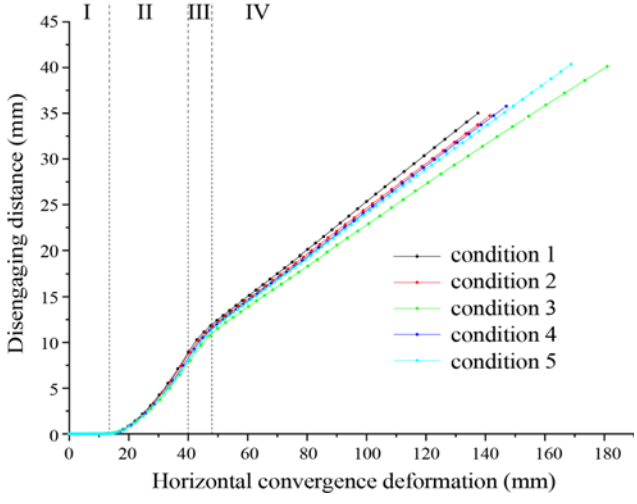

Fig. 22. Relationship between Disengaging Distance and Deformation

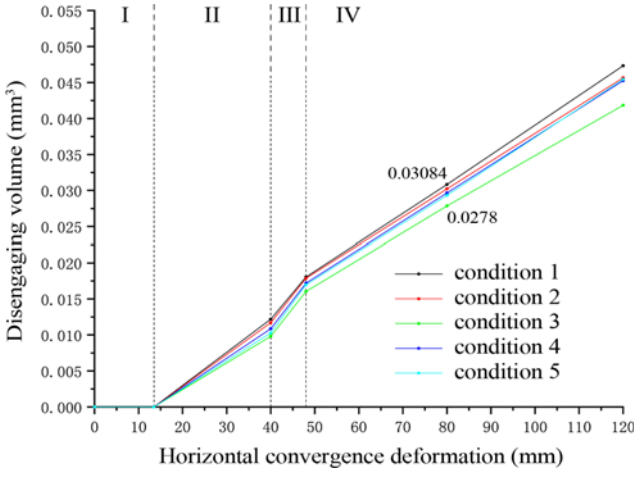

Fig. 24. Relationship between Disengaging Volume and Deformation

tunnel. Different from the development of the disengaging ratio, when the disengaging rate no longer increases, the distance between the edge of the invert tunnel and the segment is still increasing due to the continuous increase of the tunnel deformation. Therefore, the disengaging distance is still increasing.

8. Relationship between Disengaging Volume and Deformation

As shown in the red area of Fig. 23, the disengaging volume is the volume of the gap between the bottom of the invert filling and the segment after disengaging. Taking the deformation of the curve division in Fig. 22 as the control point, the disengaging volume of the single-ring shield tunnel under five conditions is extracted, as shown in Fig. 24. The variation trend of the disengaging volume of each condition is the same, but the growth rate is different. The trend of disengaging volume is similar to that disengaging distance.

Combined with the analysis in Section 4, the faster the development of deformation, the slower the growth rate of the disengaging distance, and the smaller the disengaging volume under the same deformation. When the horizontal convergence deformation reaches 80 mm, the disengaging volume in each ring of shield tunnel is 0.0278 m^3 in condition 3 and 0.0308 m^3 in condition 1. This study has obtained the disengaging volume of the invert filling under different deformations of shield tunnel, which can provide a reference for the treatment of invert filling disengaging.

9. Conclusions

A 3D numerical model of a three-ring staggered assembled shield tunnel is established, which was verified by full-scale test. Cohesive element is inserted between the invert filling and tunnel segment to simulate the fracture process of invert filling-segment interface. The main conclusions are as follows.

1. The development of invert filling disengaging affects the internal forces of shield tunnel segments. During the development of tunnel deformation, the axial force at the

section of the segment where the disengaging edge is located decreases, and the bending moment accelerates rapidly. When the disengaging edge crosses the section, the axial force increases and the bending moment decrease first and then increases.

2. The relationship between the development of invert filling disengaging and the deformation of shield tunnel can be divided into four stages. Different segment assembly methods do not affect the variation of the disengaging ratio. Tensile failure occurs in 89% of the interface layer, which is the main form of invert filling disengaging.
3. The relationship between the development of disengaging distance and the deformation of shield tunnel can be divided into four stages. The growth rate of the disengaging distance increases first and then slows down. When the disengaging ratio reaches 90%, the disengaging distance increases linearly with the deformation of shield tunnel. The faster the horizontal convergent deformation develops in the segment assembly method, the slower the growth rate of the disengaging distance.
4. The faster the horizontal convergent deformation develops in the segment assembly method, the slower the growth rate of the disengaging volume. When the horizontal convergence deformation reaches 80 mm, the disengaging volume in each ring of shield tunnel is 0.0278 m^3 in condition 3 and 0.0308 m^3 in condition 1.

Acknowledgments

The present study is sponsored by the National Natural Science Foundation of China (51908428), the Natural Science Foundation of Jiangsu Province (BK20211173) and the Opening Foundation of Key Laboratory of Urban Underground Engineering of Ministry of Education, Beijing Jiaotong University (TUL2020-02).

ORCID

Hao Jin http://orcid.org/0000-0002-3075-4415

References

Bi XL, Liu X, Wang XZ, Lu L, Yang ZH (2014) Experimental investigation on the ultimate bearing capacity of continuous-jointed segmental tunnel linings. *China Civil Engineering Journal* 47(10):117-127, DOI: 10.15951/j.tmgcxb.2014.10.028 (in Chinese)

Dagorn N, Portemont G, Berthe J, Rasselet F, Bourel B, Lauro F (2021) Development of a mixed mode double cantilever beam specimen for the fracture characterization of adhesives under high displacement rate. *Engineering Fracture Mechanics* 242:107467, DOI: 10.1016/j.engfracmech.2020.107467

Dong F, Fang Q, Zhang DL, Xu HJ, Li YJ, Niu XK (2017) Analysis on defects of operational metro tunnels in Beijing. *China Civil Engineering Journal* 50(6):104-113, DOI: 10.15951/j.tmgcxb.2017.06.012 (in Chinese)

Gao CL, Zhou ZQ, Yang WM, Lin CJ, Li LP, Wang J (2019) Model test and numerical simulation research of water leakage in operating tunnels passing through intersecting faults. *Tunnelling and Underground Space Technology* 94:103134, DOI: 10.1016/j.tust.2019.103134

Gong YC, Qi TY, Huang XD, Liang X (2020) Analysis on mechanical characteristics and evolution law of stripping disease of track bed and shield segment. *Sichuan Architecture* 40(5):99-102 (in Chinese)

Han W, Jiang YJ, Luan HJ, Liu JK, Wu XL, Du YT (2020) Fracture evolution and failure mechanism of rock-like materials containing cross-flaws under the shearing effect. *Theoretical and Applied Fracture Mechanics* 110:102815, DOI: 10.1016/j.tafmec.2020.102815

Huang LC, Ma JJ, Lei MF, Liu LH, Lin YX, Zhang ZY (2020) Soil-water inrush induced shield tunnel lining damage and its stabilization: A case study. *Tunnelling and Underground Space Technology* 97:103290, DOI: 10.1016/j.tust.2020.103290

Ji CJ (2014) Study on numerical simulation and evaluation standard of ballast disengaging for metro sections. *Modern Transportation Technology* 11(6):74-77, DOI: 10.3969/j.issn.1672-9889.2014.06.021 (in Chinese)

Ji X, Chen Q (2019) Analysis on the treatment technology of bed slab fracture and void during metro operation period. *Engineering Technology and Application* 4(6):84-85, DOI: 10.19537/j.cnki.2096-2789.2019.06.036 (in Chinese)

Jin H, Tian QR, Li Z, Wang ZH (2022) Ability of vibration control using rubberized concrete for tunnel invert-filling. *Construction and Building Materials* 317:125932, DOI: 10.1016/j.conbuildmat.2021.125932

Jin H, Yu S (2022) Study on corrosion-induced cracks for the concrete with transverse cracks using an improved CDM-XFEM. *Construction and Building Materials* 318:126173, DOI: 10.1016/j.conbuildmat.2021.126173

Jin H, Yu S, Zhou SH, Xiao JH (2018) Research on mechanics of longitudinal joint in shield tunnel by the nonlinear spring equivalent method. *KSCE Journal of Civil Engineering* 23(2):902-913, DOI: 10.1007/s12205-018-0667-5

Jin YF, Zhu BQ, Yin ZY, Zhang DM (2019) Three-dimensional numerical analysis of the interaction of two crossing tunnels in soft clay. *Underground Space* 4(4):310-327, DOI: 10.1016/j.undsp.2019.04.002

Li YJ, Xu HJ, Song GX, Ni KQ, Gao C (2020a) Treatment technology of monolithic ballast disengaging in shield tunnel. *China Civil Engineering Journal* 53(S1):119-123, DOI: 10.15951/j.tmgcxb.2020.s1.020 (in Chinese)

Li CD, Zhang W, Wang XM, Pan B, Zhu HH, Spencer BF (2020b) Modeling dynamic responses of a cross-river road shield tunnel under stochastic vehicle loads. *Tunnelling and Underground Space Technology* 102:103432, DOI: 10.1016/j.tust.2020.103432

Liang RZ, Wu WB, Yu F, Jiang GS, Liu JW (2018) Simplified method for evaluating shield tunnel deformation due to adjacent excavation. *Tunnelling and Underground Space Technology* 71:94-105, DOI: 10.1016/j.tust.2017.08.010

Liu F, He MD, Yu L, Liu Y, Li YJ, Wu LS (2015) Measurement on the separation of monolithic roadbed from tunnel by hydrostatic leveling sensor. *China Civil Engineering Journal* 48(S2):356-360 (in Chinese)

Liu JW, Shi CH, Wang ZX, Lei MF, Zhao D, Cao CY (2021) Damage mechanism modelling of shield tunnel with longitudinal differential deformation based on elastoplastic damage model. *Tunnelling and Underground Space Technology* 113:103952, DOI: 10.1016/j.tust.2021.103952

Molins C, Arnau O (2011) Experimental and analytical study of the structural response of segmental tunnel linings based on an in situ loading test. *Tunnelling and Underground Space Technology* 26(6):

764-777, DOI: 10.1016/j.tust.2011.05.002

Rabczuk T, Belytschko T (2004) Cracking particles: A simplified meshfree method for arbitrary evolving cracks. *International Journal for Numerical Methods in Engineering* 61(13):2316-2343, DOI: 10.1002/nme.1151

Rabczuk T, Belytschko T (2007) A three-dimensional large deformation meshfree method for arbitrary evolving cracks. *Computer Methods in Applied Mechanics and Engineering* 196(29-30):2777-2799, DOI: 10.1016/j.cma.2006.06.020

Rabczuk T, Zi G, Bordas S, Nguyen-Xuan H (2008) A geometrically non-linear three-dimensional cohesive crack method for reinforced concrete structures. *Engineering Fracture Mechanics* 75(16):4740-4758, DOI: 10.1016/j.engfracmech.2008.06.019

Shao H, Huang HW, Zhang DM, Wang RL (2016) Case study on repair work for excessively deformed shield tunnel under accidental surface surcharge in soft clay. *Chinese Journal of Geotechnical Engineering* 38(6):1036-1043, DOI: 10.11779/CJGE201606009 (in Chinese)

Shen SL, Wu HN, Cui YJ, Yin ZY (2014) Long-term settlement behaviour of metro tunnels in the soft deposits of Shanghai. *Tunnelling and Underground Space Technology* 40:309-323, DOI: 10.1016/j.tust.2013.10.013

Shi CH, Cao CY, Lei MF, Peng LM, Ai HJ (2016) Effects of lateral unloading on the mechanical and deformation performance of shield tunnel segment joints. *Tunnelling and Underground Space Technology* 51:175-188, DOI: 10.1016/j.tust.2015.10.033

Wang SM, Wang XM, Chen B, Fu YB, Jian YQ, Lu XX (2020) Critical state analysis of instability of shield tunnel segment lining. *Tunnelling and Underground Space Technology* 96:103180, DOI: 10.1016/j.tust.2019.103180

Wang RL, Zhang DM (2013) Mechanism of transverse deformation and assessment index for shield tunnels in soft clay under surface surcharge. *Chinese Journal of Geotechnical Engineering* 35(6):1092-1101 (in Chinese)

Wu HN, Shen SL, Chen RP, Zhou A (2020) Three-dimensional numerical modelling on localised leakage in segmental lining of shield tunnels. *Computers and Geotechnics* 122:103549, DOI: 10.1016/j.compgeo.2020.103549

Wu HN, Shen SL, Liao SM, Yin ZY (2015) Longitudinal structural modelling of shield tunnels considering shearing dislocation between segmental rings. *Tunnelling and Underground Space Technology* 50:317-323, DOI: 10.1016/j.tust.2015.08.001

Wu HN, Shen SL, Yang J (2017) Identification of tunnel settlement caused by land subsidence in soft deposit of Shanghai. *Journal of Performance of Constructed Facilities* 31(6), DOI: 10.1061/(asce)cf.1943-5509.0001082

Xiao JZ, Liu HR, Ding T (2021) Finite element analysis on the anisotropic behavior of 3D printed concrete under compression and flexure. *Additive Manufacturing* 39:101712, DOI: 10.1016/j.addma.2020.101712

Yan QX, Xu YJ, Zhang WL, Geng P, Yang WB (2018) Numerical analysis of the cracking and failure behaviors of segmental lining structure of an underwater shield tunnel subjected to a derailed high-speed train impact. *Tunnelling and Underground Space Technology* 72:41-54, DOI: 10.1016/j.tust.2017.11.002

Yi HY, Qi TY, Qian WP, Lei B, Pu BR, Yu YY, Liu YX, Li ZY (2019) Influence of long-term dynamic load induced by high-speed trains on the accumulative deformation of shallow buried tunnel linings. *Tunnelling and Underground Space Technology* 84:166-176, DOI: 10.1016/j.tust.2018.11.005

Zhang JH, Li Y, Liu XW, Sun ZZ, Cao GQ (2020) Statistical analysis of shield tunnel disease based on horizontal convergence in soft clay. *China Civil Engineering Journal* 53(S1):124-130, DOI: 10.15951/j.tmgcxb.2020.s1.021 (in Chinese)

Zheng YL, Han WX, Tong QH, Yang LF, Pan J (2005) Study on longitudinal crack of shied tunnel segment joint due to asymmetric settlement in soft soil. *Chinese Journal of Rock Mechanics and Engineering* 24(24):4552-4558, DOI: 10.3321/j.issn:1000-6915.2005.24.025 (in Chinese)

Zhu B (2014) Research on the law and controlled limit value of transverse deformation for shield tunnel in soft clay. *Journal of Railway Engineering Society* 31(9):71-76, DOI: 10.3969/j.issn.1006-2106.2014.09.014 (in Chinese)